Acta Mechanica 165, 189–206 (2003)
DOI 10.1007/s00707-003-0013-x

Acta Mechanica
Printed in Austria

Propulsive performance and vortex shedding of a foil in flapping flight

X.-Y. Lu, J.-M. Yang, and **X.-Z. Yin,** Hefei, China

Received January 9, 2003; revised March 10, 2003
Published online: October 30, 2003

Summary. The propulsive performance and vortex shedding of an oscillating foil, which mimics biological locomotion, are investigated based on a computational fluid dynamics analysis. The objectives of this study are to investigate unsteady forces, in particular a thrust force, for the foil in pitching and plunging motion, and to deal with the relations of the propulsive performance with leading-edge vortex structure and vortex shedding in the near wake. The two-dimensional incompressible Navier–Stokes equations in the vorticity and stream-function formulation are solved by fourth-order essentially compact finite difference schemes for the space derivatives and a fourth-order Runge-Kutta scheme for the time advancement. To reveal the mechanism of the propulsive performance, the unsteady forces and the shedding of the leading- and trailing-edge vortices of the foil in the pitching and plunging motion are analyzed. Based on our calculated results, three types of the leading-edge vortex shedding, which have an effective influence on the vortex structures in the wake of the oscillating foil, are identified. The effects of some typical factors, such as the frequency and amplitude of the oscillation, the phase difference between the pitching and plunging motions, and the thickness ratio of the foil, on the vortex shedding and the unsteady forces are discussed.

1 Introduction

Insects and fish have experienced a billions-year process of evolution with natural selection for their survival and have developed their superior and complete performance of flight and swimming. Those animals act under their neural control with their muscle contraction as a motor to transform the biochemical energy to mechanical energy and then implement their wing-flapping or body-undulating propulsion. We are interested in understanding the design concepts of these living machines, which include the neural science, muscle mechanics, morphology diversity and locomotion patterns (kinematics), propulsion and its control studies (dynamics), energy costs and efficiency (energetics), biological material properties, etc. All these are involved in a discipline of flying and swimming biomechanics. Pioneering work in the biomechanics of animal locomotion in the quasi-steady limit was done by Weis-Fogh et al. [1] and Lighthill [2] among others. Comprehensive reviews of much previous work can be found in the literature [3]–[7].

Usually, flapping motion is a basic mode of locomotion in insects, birds, and fish. Thrust and lift are generated when the flapping wings or tails interact with the surrounding fluids. Because of the highly unsteady nature of viscous flow around a flapping wing, it is needed to understand the physical mechanism and vortex shedding in unsteady viscous flow, which is crucial to the locomotion performance. In particular, an oscillating foil has often been

employed as a typical model to deal with the flapping motion to mimic biological locomotion.

Some work on this subject has been theoretically, experimentally and computationally carried out. Theoretical analyses including the vortex panel method and the unsteady lifting-line theory have been performed for bird flight [8] and fish swimming [3], [9], [10]. A detailed review of various theoretical methods has been given by Smith et al. [11]. Experiments on oscillating foils have exhibited the existence of optimal parameters for the generation of an effective thrust. Triantafyllou et al. [12] studied experimentally the wake mechanics for thrust generation in oscillation foils. Anderson et al. [13] and Gursul and Ho [14] examined the high propulsive efficiency of oscillating foils at a certain frequency. Some recent experimental work has been performed to investigate the leading-edge vortices in insect flight by Ellington et al. [15], as well as the wing rotation and the aerodynamic basis of insect flight by Dickenson et al. [16]. In particular, extensive works [15]–[19] have explored the mechanism of the leading-edge vortices which plays an important role to generate unconventional forces in insect flight.

By use of computational fluid dynamics methods, a two-dimensional hovering flight was numerically computed by Gustafson et al. [20], and their calculated results were in qualitative agreement with some available experimental data. Liu et al. [21], [22] applied a method of pseudo-compressibility to compute viscous flow around a three-dimensional rigid wing, and examined the axial flows associated with the leading-edge vortex as observed in the experiments by Ellington et al. [15]. Wang [23] performed a two-dimensional computation of a foil in flapping motion to reveal the frequency selection in forward insect flapping flight. Hall et al. [24] examined the power requirements for flapping flight. Recently, Sun et al. [25], [26] investigated numerically the unsteady aerodynamics of a model fruit fly wing in flapping motion, and the lift and power requirements for hovering flight.

In this work, the goals of our study are to investigate the unsteady forces of the foil in pitching and plunging motion, as well as to deal with the relation of the propulsive performance with the vortex structure evolution near the foil and vortex shedding in the near wake. In this study, viscous flow past a foil in pitching and plunging motion, that is capable of mimicing biological locomotion, is numerically investigated for a wide range of the computational parameters. The two-dimensional incompressible Navier–Stokes equations in the vorticity and stream-function formulation are solved by a fourth-order essentially compact finite difference scheme, developed by E and Liu [27], for the space derivatives, and a fourth-order Runge-Kutta scheme for the time advancement. To explore the mechanism of the propulsive performance, the unsteady forces and the shedding of the leading- and trailing-edge vortices are analyzed for the foil in the pitching and plunging motion.

This paper is organized as follows. The mathematical formulations are described in Sect. 2. The numerical method is briefly given in Sect. 3. In Sect. 4, some typical results for unsteady force and vortex shedding are discussed. Finally, concluding remarks are summarized in Sect. 5.

2 Governing equations

A sketch of a foil in pitching and plunging motion to mimic biological locomotion is illustrated in Fig. 1. In this study, the frame is fixed with the foil motion, and the two-dimensional incompressible Navier–Stokes equations in the vorticity and stream-function formulation are employed. To nondimensionalize the governing equations, the chord length of the foil c is used

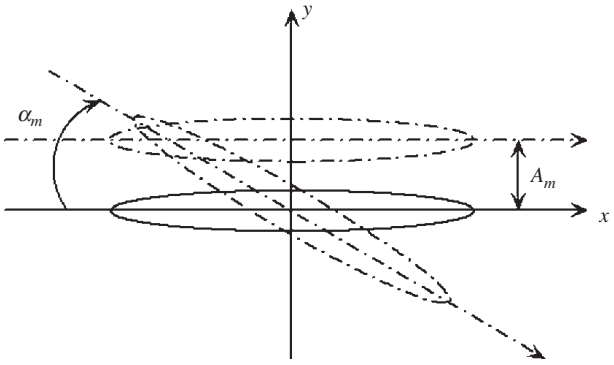

Fig. 1. Sketch of a foil in plunging and pitching motion

as the length scale, the free-stream velocity U as the velocity scale. The nondimensional governing equations are thus given by

$$\frac{\partial\omega}{\partial t}+\frac{\partial\psi}{\partial y}\frac{\partial\omega}{\partial x}-\frac{\partial\psi}{\partial x}\frac{\partial\omega}{\partial y}=\frac{1}{\mathrm{Re}}\nabla^2\omega-2\frac{d\Omega}{dt}, \tag{1}$$

$$\nabla^2\psi=-\omega, \tag{2}$$

where ω and ψ represent the vorticity and stream-function, respectively. Ω is the rotation speed of the pitching oscillation. Re is the Reynolds number, defined as $\mathrm{Re}=Uc/v$, and v is the kinematic viscosity. Based on the stream-function, the velocity is obtained by

$$u=\frac{\partial\psi}{\partial y},\quad v=-\frac{\partial\psi}{\partial x}, \tag{3}$$

where u and v represent the velocity components in x- and y-directions, as shown in Fig. 1, respectively.

When the Navier-Stokes equations (1), (2) in the frame fixed with the foil motion are solved, an additional term due to the Coriolis force occurs in Eq. (1) for the pitching motion, and no fictitious force appears in the vorticity equation (1) for the plunging motion considered here. The no-slip and no-penetration boundary conditions at the foil are enforced explicitly through the vorticity and stream-function boundary condition, respectively. In the far field, the boundary condition on the stream-function is given by the potential flow [23].

The motion of the foil consists of pitching and plunging oscillation. The plunging oscillation is described by

$$h=A_m\sin(2\pi ft+\theta), \tag{4}$$

and the pitching oscillation by

$$\alpha=\alpha_m\sin(2\pi ft+\theta+\phi), \tag{5}$$

where A_m and α_m are the nondimensional plunging and pitching amplitudes, respectively, f represents the nondimensional oscillation frequency, and θ and ϕ denote the initial phase and the phase difference between the pitching and plunging oscillations. To simplify the present calculation, the same frequency f is used in both the pitching and plunging oscillations.

3 Numerical methods

In this study, a fourth-order essentially compact finite difference scheme, developed by E and Liu [27], is employed to solve the incompressible Navier-Stokes equations. To achieve a fourth-

order spatial accuracy, an advantage of the scheme is that two Poisson equations only need to be solved by use of the FFT technique at each time step [27]. By using the Navier-Stokes equations in the vorticity-stream function formulation, the vorticity boundary condition is explicitly enforced to satisfy the no-slip boundary condition. To discretize the time derivative in Eq. (1), a fourth-order Runge-Kutta scheme is employed for the time advancement. The discretization formulations have been described in detail in [27].

4 Results and discussion

In this study, an elliptic foil is used, and a conformal map is employed for grid generation with a grid number 256×256 in the radial and circumferential directions, respectively. The computational domain is about $10c$ in the radial direction, and the time step is 0.0002 based on the computation stability condition. Extensive convergence checks with different grid sizes and time steps have been undertaken. It has been determined that the computed results are independent of the time steps and the grid sizes used in the present calculation. Some typical results are shown in the following discussion.

To deal systematically with the mechanism of propulsive performance and vortex shedding of a foil in the pitching and plunging motion, the computation parameters are chosen as follows. The Reynolds number is $\mathrm{Re} = 10^3$, the thickness ratio of the foil $\lambda = 0.0625 \sim 0.5$. In Eqs. (4) and (5), the plunging amplitude $A_m = 0.08 \sim 0.32$, the pitching amplitude $\alpha_m = 5^\circ \sim 20^\circ$, the frequency of the oscillation $f = 0.5 \sim 4$, the phase difference $\phi = 45^\circ \sim 225^\circ$, and the initial phase $\theta = 180^\circ$. To demonstrate the effects of those computational parameters, e.g., λ, A_m, α_m, f and ϕ, on the vortex shedding and the corresponding time-dependent forces, some typical results are mainly discussed.

Here, we first depict the sketch of three types of the leading-edge vortex shedding based on the present calculated results, as shown in Fig. 2, where the leading-edge vortex evolution is only shown in half-cycle of the oscillation. In Fig. 2a, denoted as the mode-1, the leading-edge vortex pairs with another vortex and passes over the leading-edge of the foil from one side to another side of the foil. The vortex evolution is helpful to generate a thrust force due to the formation of the lower-pressure distribution along the leading-edge region induced by the

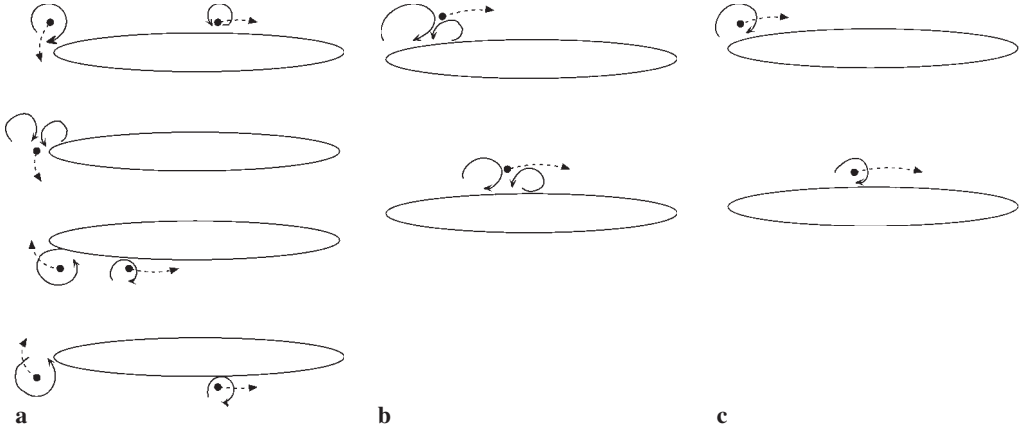

Fig. 2. Sketch of three types of the leading-edge vortex shedding evolution: **a** Mode-1; **b** Mode-2; **c** Mode-3

vortex. In the mode-2 (Fig. 2b), the leading-edge vortex pairs with another vortex to form a vortex-pair, which is shedding downstream along the foil. In Fig. 2c (i.e., the mode-3), a single of the leading-edge vortex is shedding downstream. The evolution of the leading-edge vortex has an effective influence on the vortex structures in the wake of the foil. In our previous work to investigate the vortex control of an airfoil by using small perturbation near the leading-edge region of the airfoil [28], the leading-edge vortex evolution has an effective influence on the vortex shedding and vortex structures in the wake of the airfoil. According to our extensive calculations for different parameters, if the leading-edge vortex development behaves as the mode-1 (Fig. 2a) or mode-2 (Fig. 2b), a reverse Karman vortex-street is formed in the wake of the foil due to the interaction of the leading-edge vortex with the trailing-edge shedding vortex. However, if the leading-edge vortex evolution behaves as the mode-3 (Fig. 2c), a classic Karman vortex wake is generated.

Figure 3 shows the time-dependent drag and lift coefficients for the plunging oscillation at $A_m = 0.16, f = 1, \lambda = 0.125$. The lift coefficient C_L varies symmetrically about zero, thus the time-averaged lift force is zero as expected from the symmetric flapping. The frequency of C_D is twice that of C_L, because the drag is generated in both the up and down oscillations. The drag coefficient C_D variation is asymmetric about the zero value, because the fore-and-aft symmetry is broken due to the free-stream velocity. The time-averaged drag coefficient $\bar{C}_D$ is -0.39 approximately. Here, we define that a negative value of $\bar{C}_D$ corresponds to a thrust in the mean

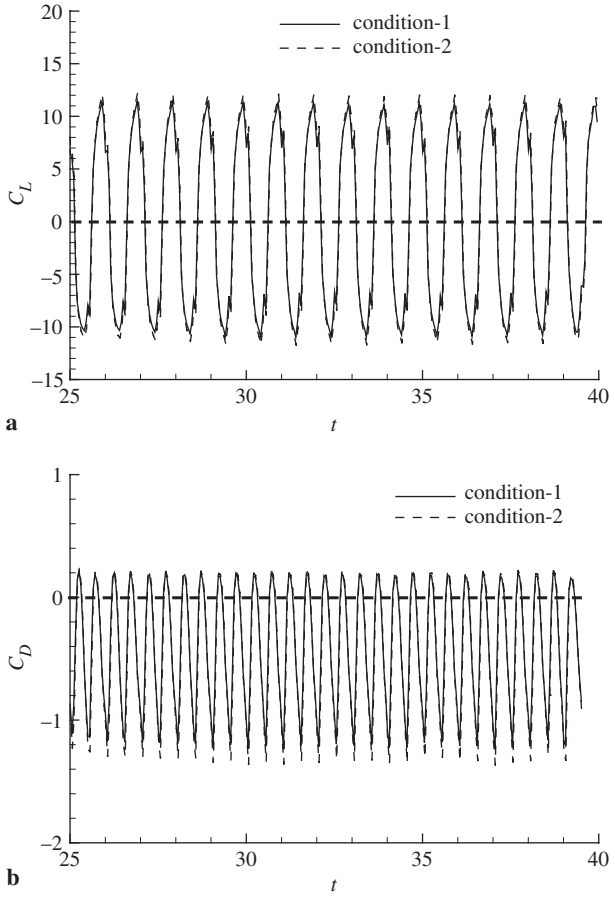

Fig. 3. Time-dependent lift and drag coefficients for the plunging oscillation at $A_m = 0.16$, $f = 1$ and $\lambda = 0.125$: **a** lift coefficient C_L; **b** drag coefficient C_D. Condition-1: grid number 256×256, time step 0.0002; Condition-2: grid number 512×512, time step 0.0001

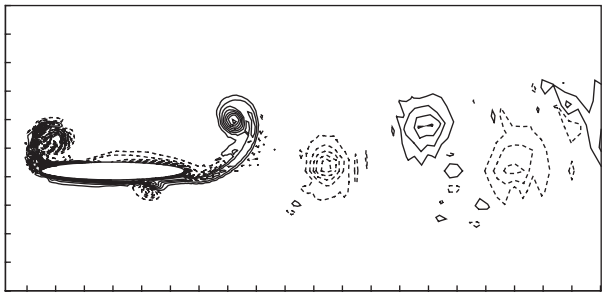

a

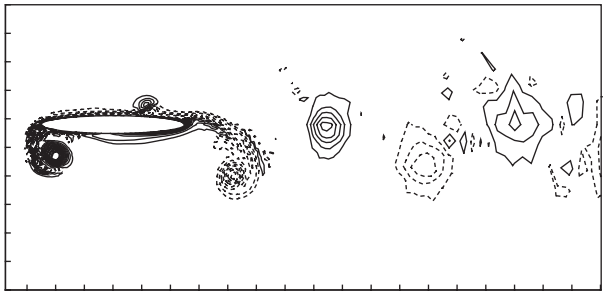

b

Fig. 4. Instantaneous vorticity contours at $A_m = 0.16$, $f = 1$ and $\lambda = 0.125$: **a** $T/4$; **b** $3T/4$. Here, solid lines represent positive values and dashed lines negative values. The increment of the contours is 5

forward direction. Thus, the mean thrust coefficient in this case is 0.39. To demonstrate that the computed results are independent of the time steps and the grid sizes, the results calculated by different grid numbers and time steps are also shown in Fig. 3.

To analyse the mechanism of the thrust generation, the qualitative feature of the associated vortex shedding is examined. From instantaneous vorticity contours in Fig. 4, a reverse Karman vortex-street is formed in the wake of the foil, where the vortices in the wake rotate in the opposite direction compared to a classic Karman vortex wake. Hence, the induced flow has a component moving backward with respect to the foil to generate the thrust [2], [3]. To understand vortex evolution more clearly near the foil, Fig. 5 shows the vorticity contours at different phases in one cycle. During the first-half cycle, the foil is moving downward. A negative leading-vortex LV_{N1} is formed (Fig. 5a) and paired with another positive leading-vortex LV_{P0} to form a vortex pair (i.e., $LV_{P0} + LV_{N1}$) in Fig. 5b, here, the positive vortex represents a counter-clockwise vortex and the negative one is a clockwise vortex. Meanwhile, a negative vortex (LV_{N0}) formed in the previous cycle moves downstream along the lower-side of the foil, and a positive trailing-vortex TV_{P1} is generated. Note that the vortex pair ($LV_{P0} + LV_{N1}$) rotates in Fig. 5c and separates again in Fig. 5d. Then, it is interesting to find that the vortex LV_{P0} moves downstream along the upper-side of the foil, and the vortex LV_{N1} is passing over the leading-edge of the foil from the upper-side to the lower-side of the foil. The vortex (LV_{N1}) evolution is helpful to generate a thrust force due to the formation of the lower-pressure distribution induced by the vortex. In Fig. 5d, when a positive leading-vortex LV_{P1} is generated, the positive trailing-vortex TV_{P1} is shedding downstream, and a negative trailing-vortex TV_{N1} is formed. In the following half-cycle, the foil is oscillating upward. As expected,

Fig. 5. Instantaneous vorticity contours at $A_m = 0.16$, $f = 1$ and $\lambda = 0.125$: **a** $T/8$; **b** $2T/8$; **c** $3T/8$; **d** $4T/8$; **e** $5T/8$; **f** $6T/8$; **g** $7T/8$; **h** $8T/8$. Solid lines represent positive values and dashed lines negative values. The increment of the contours is 5

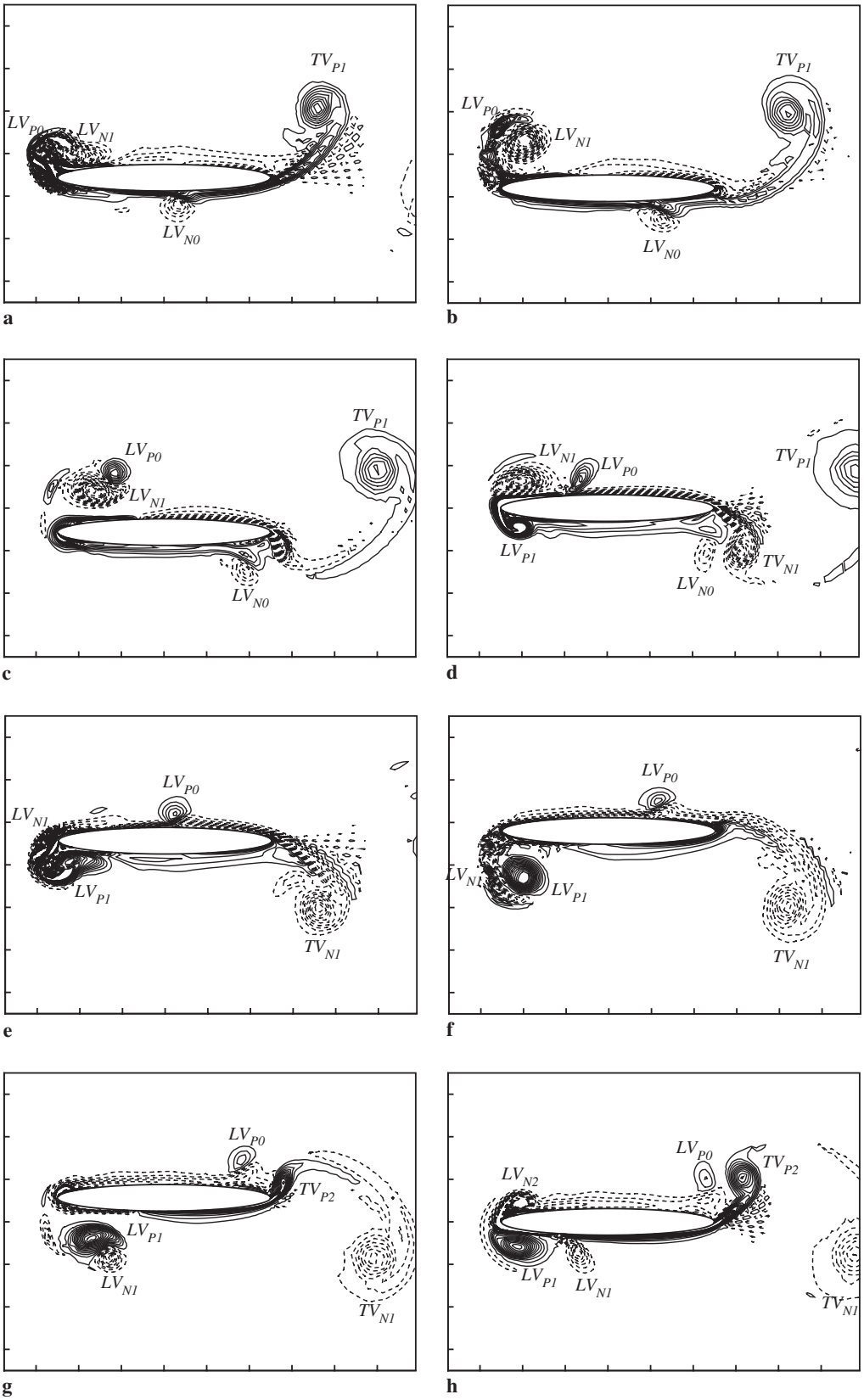
TV_{P1}
LV_{P0}
LV_{N1}
LV_{N0}
a
TV_{P1}
LV_{P0}
LV_{N1}
LV_{N0}
b
TV_{P1}
LV_{P0}
LV_{N1}
LV_{N0}
c
LV_{N1}
LV_{P0}
TV_{P1}
LV_{P1}
LV_{N0}
TV_{N1}
d
LV_{P0}
LV_{N1}
LV_{P1}
TV_{N1}
e
LV_{P0}
LV_{N1}
LV_{P1}
TV_{N1}
f
LV_{P0}
TV_{P2}
LV_{P1}
LV_{N1}
TV_{N1}
g
LV_{P0}
TV_{P2}
LV_{N2}
LV_{P1}
LV_{N1}
TV_{N1}
h

the vortex evolution is repeated in the opposite direction. In Figs. 5e and 5f, the leading-vortex LV_{N0} coalesces with the trailing-vortex TV_{N1} to shed downstream. Meanwhile, the negative vortex LV_{N1} formed in the upper-side of the foil is paired with the vortex LV_{P1} to form a vortex pair (i.e., $LV_{P1} + LV_{N1}$) in Figs. 5f and 5g. When the trailing-vortex TV_{N1} is shedding downstream in Fig. 5g, another positive vortex TV_{P2} is gradually generated. Then, the vortex pair ($LV_{P1} + LV_{N1}$) is separated in Fig. 5h. The vortex LV_{N1} moves downstream along the lower-side of the foil and corresponds to the vortex LV_{N0} in Fig. 5a. The vortex LV_{P1} moves over the leading-edge from the lower-side to the upper-side of the foil and corresponds to the vortex LV_{P0} in Fig. 5a. Based on the above description, it is a typical Mode-1 evolution of the leading-edge vortex. In the near wake of the foil, as shown in Fig. 4, a reverse Karman vortex-street is formed when the vortices generated from the foil shed into the downstream. In the following oscillation cycle, the vortex evolution is repeated as described above.

Further, to deal with the effect of the amplitude of plunging oscillation on the force and vortex shedding, Fig. 6 shows the time-dependent drag and lift coefficients for the plunging oscillation at $A_m = 0.08, f = 1, \lambda = 0.125$. As expected, the time-averaged lift coefficient $\bar{C}_L$ is zero approximately. The time-averaged drag coefficient $\bar{C}_D$ is 0.12 approximately, and a classic Karman vortex-street is observed in the wake. To demonstrate the vortex patterns near the foil, the vorticity contours at several phases in one cycle are shown in Fig. 7. When the foil is oscillating downward, a negative leading-vortex LV_{N1} is generated in Fig. 7a, and a positive leading-vortex LV_{P0} formed in the previous cycle is moving downstream along the lower-side of

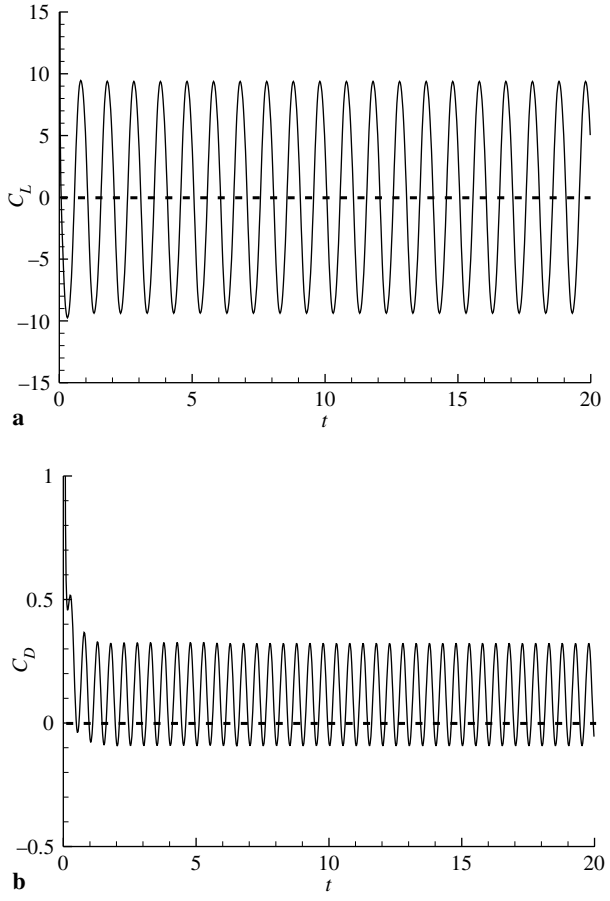

Fig. 6. Time-dependent lift and drag coefficients for the plunging oscillation at $A_m = 0.08$, $f = 1$ and $\lambda = 0.125$: **a** lift coefficient C_L; **b** drag coefficient C_D

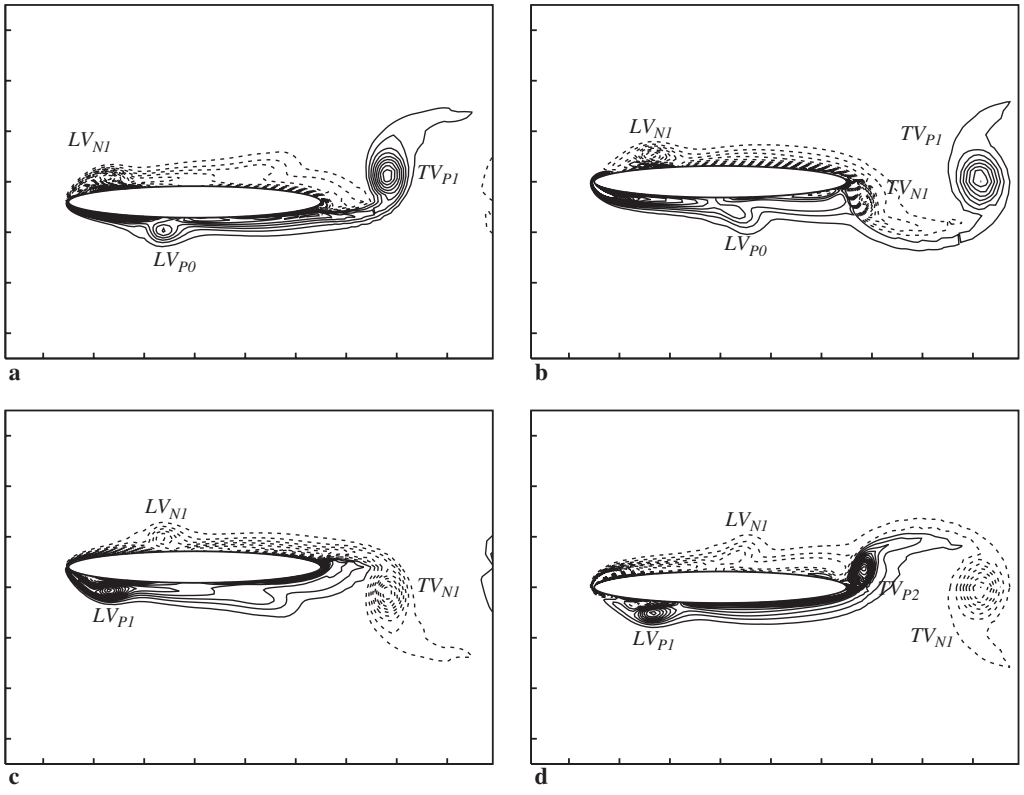

Fig. 7. Instantaneous vorticity contours at $A_m = 0.08, f = 1$ and $\lambda = 0.125$: **a** $T/4$; **b** $2T/4$; **c** $3T/4$; **d** $4T/4$. Solid lines represent positive values and dashed lines negative values. The increment of the contours is 4

the foil, as shown in Fig. 7a and b. Meanwhile, a positive trailing-vortex TV_{P1} is shedding into the wake, and another negative TV_{N1} is gradually generated. When the foil is oscillating upward, a positive leading-vortex LV_{P1} is formed and moves downstream in Fig. 7c and d. When the trailing-vortex TV_{N1} is shedding, a positive trailing-vortex TV_{P2} is formed again. As demonstrated, the evolution of the leading-edge vortex belongs to the Mode-3 (Fig. 2c). Finally, the vortices shed from the foil form a Karman vortex-street in the near wake of the foil.

Based on the calculated results, Fig. 8 exhibits the time-averaged drag coefficient $\bar{C}_D$ versus the amplitude of plunging oscillation at $f = 1$, $\lambda = 0.125$. It can be found that an effective thrust force is generated at the amplitude $A_m = 0.15 \sim 0.25$ approximately. Figure 8 reasonably depicts the character of $\bar{C}_D$ with A_m. In a limiting case with $A_m \to 0$, the foil is stationary and always undergoes a drag force. Thus, as shown in Fig. 8, when A_m decreases from $A_m = 0.16$, $\bar{C}_D$ increases from negative to positive value. However, when A_m increases further from $A_m = 0.2$, the flow structure becomes more complicated and hardly to form a well-organized reverse Karman vortex-street in the near wake of the foil; $\bar{C}_D$ thus increases gradually, or the corresponding thrust decreases. This behavior is consistent with the results by Wang [23] and the data of forward dragonfly flight by Norberg [29].

Although frequency selection in forward flapping flight was investigated numerically by Wang [23], an analysis is briefly given to illustrate the effect of the frequency of plunging oscillation on the vortex shedding near the foil and the corresponding time-dependent forces. Figures 9 and 10 show the time-dependent lift and drag coefficients for $f = 0.5$ and 2 at

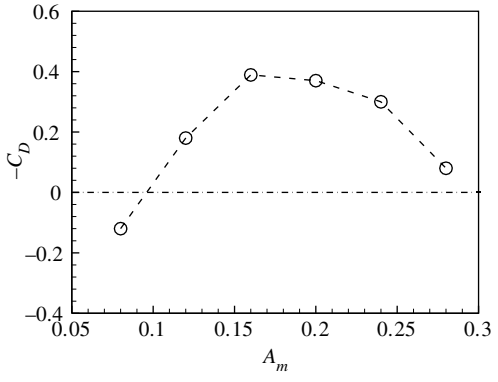

Fig. 8. Time-averaged drag coefficient versus the amplitude of plunging oscillation at $f = 1$ and $\lambda = 0.125$

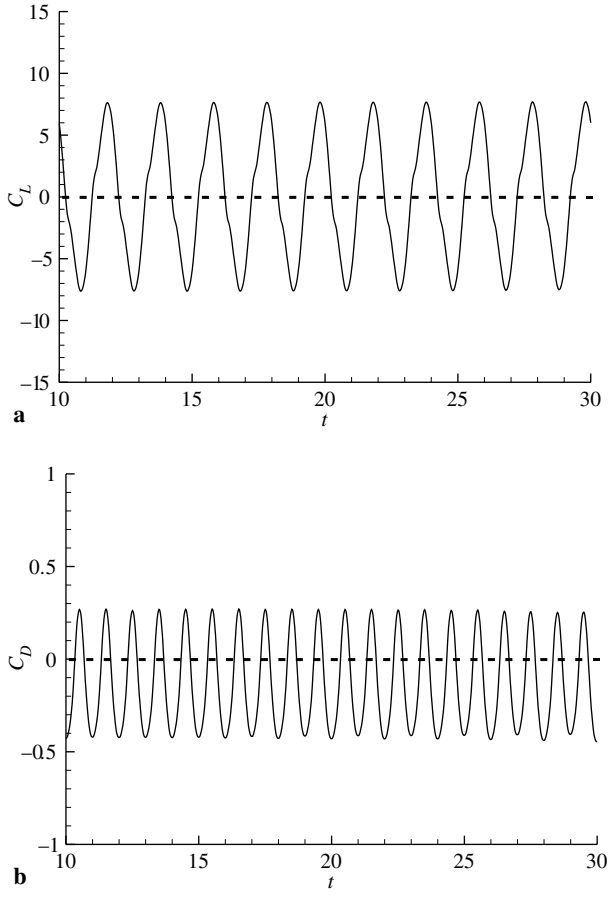

Fig. 9. Time-dependent lift and drag coefficients for the plunging oscillation at $A_m = 0.16$, $f = 0.5$ and $\lambda = 0.125$: **a** lift coefficient C_L; **b** drag coefficient C_D

$A_m = 0.16$ and $\lambda = 0.125$, respectively. The lift coefficients C_L vary about the zero mean value. The amplitude of C_L at $f = 2$ is higher than that at $f = 0.5$ due to the inertial effect of plunging oscillation. Both for $f = 0.5$ and 2, thrust force is generated because the time-averaged drag coefficient ($\bar{C}_D$) is negative. From the instantaneous vorticity contours (not shown here), it is also found that the leading-edge vortex development behaves as the Mode-1 (Fig. 2a), and the reverse Karman vortex-street is observed in the wake of the foil for the corresponding conditions in Figs. 9 and 10.

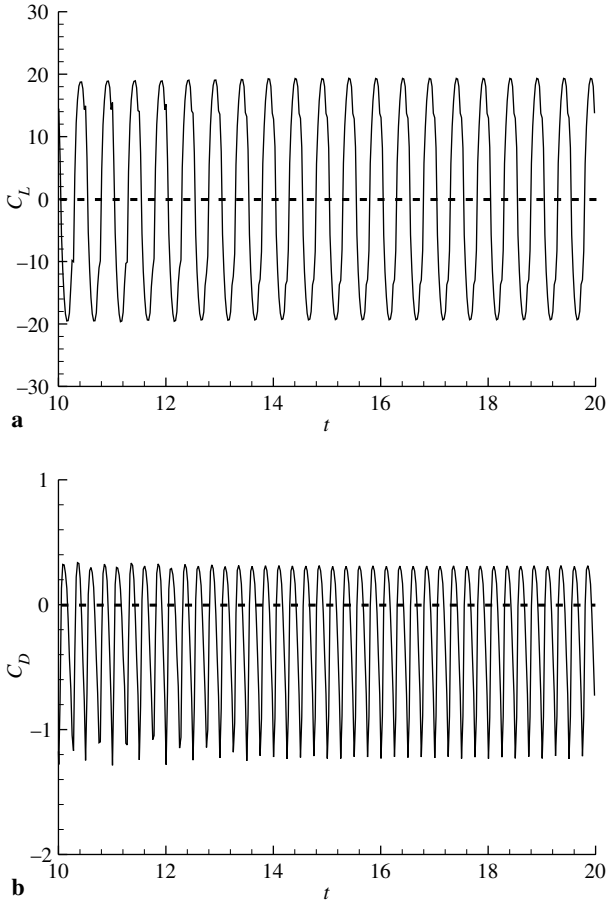

Fig. 10. Time-dependent lift and drag coefficients for the plunging oscillation at $A_m = 0.16$, $f = 2$ and $\lambda = 0.125$: **a** lift coefficient C_L; **b** drag coefficient C_D

The frequency of the oscillation is usually a key parameter and has an effective influence on the vortex shedding and vortex structure in the wake of the foil for flapping flight [23] and unsteady vortex control [28]. To demonstrate the effect of frequency on the force, Fig. 11 depicts the time-averaged drag coefficient $\bar{C}_D$ versus the frequency of plunging oscillation at $A_m = 0.16$, $\lambda = 0.125$. The character of $\bar{C}_D$ varying with the frequency is consistent with the results by Wang [23]. From Fig. 11, it is found that an effective thrust force is generated in a region of $f = 1 \sim 2$ approximately.

To illustrate the effect of the thickness ratio of the foil (λ) on the force and vortex shedding, several different thickness ratios are calculated. As shown in Fig. 3, the time-averaged drag coefficient $\bar{C}_D$ is −0.39 approximately at $\lambda = 0.125$. Further, Fig. 12 shows the time-dependent drag coefficient for $\lambda = 0.25$ and 0.3, respectively. At $\lambda = 0.25$ (Fig. 12a), $\bar{C}_D$ is 0.065 approximately, where a vortex-street ranking near as one line is formed. With increasing λ, such as at $\lambda = 0.3$ (Fig. 12b), $\bar{C}_D$ is 0.25 approximately, where a classic Karman vortex-street is observed in the wake of the foil, and the leading-edge vortex development behaves as the Mode-3 (Fig. 2c). If λ increases further, as a typical case with $\lambda = 1$, i.e., a transversely oscillating circular cylinder in a uniform flow, it is well known that a drag force is always formed [30]. Based on the present calculated results, Fig. 13 shows the time-averaged drag coefficient $\bar{C}_D$ versus the thickness ratio of the foil at $f = 1$ and $A_m = 0.16$. When the thickness ratio of the foil lays in a region of $\lambda = 0.1 \sim 0.15$, an effective thrust force is generated.

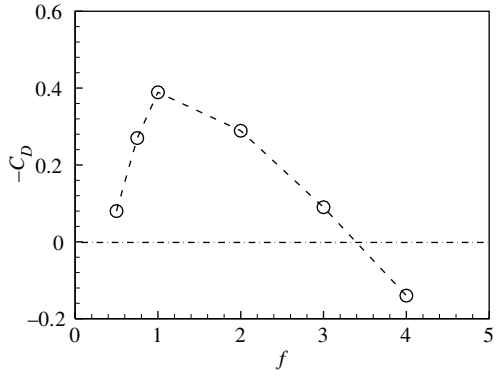

Fig. 11. Time-averaged drag coefficient versus the frequency of plunging oscillation at $A_m = 0.16$ and $\lambda = 0.125$

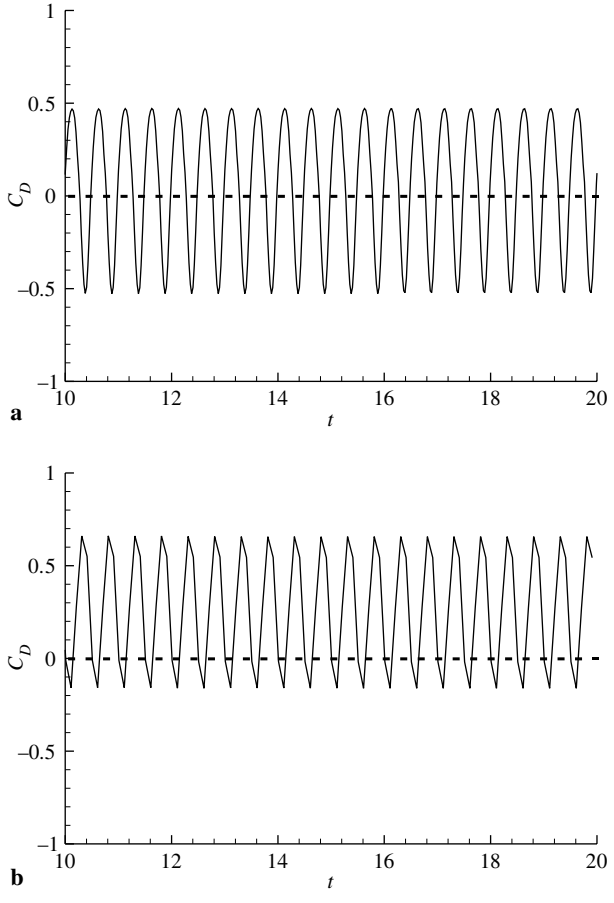

Fig. 12. Time-dependent drag coefficient at $A_m = 0.16$, $f = 0.5$, $\lambda = 0.25$ and 0.3: **a** $\lambda = 0.25$; **b** $\lambda = 0.3$

Further, a foil in a pitching oscillation around its mid-chord is considered. Figure 14 exhibits the lift and drag coefficients versus time at $\alpha_m = 10^\circ$, $\lambda = 0.125$ and $f = 1$. The lift coefficient C_L varies symmetrically about zero from the symmetric pitching oscillation foil. The frequency of C_D is twice that of C_L, because the drag is generated in both the up and down oscillations. It is found that the time-averaged drag coefficient $\bar{C}_D$ is positive, correspondingly the leading-edge vortex development behaves as the Mode-3 (Fig. 2c), and a classic Karman vortex-street is formed in the wake of the pitching foil. Several cases for $\alpha_m = 5^\circ \sim 20^\circ$ are calculated, and the

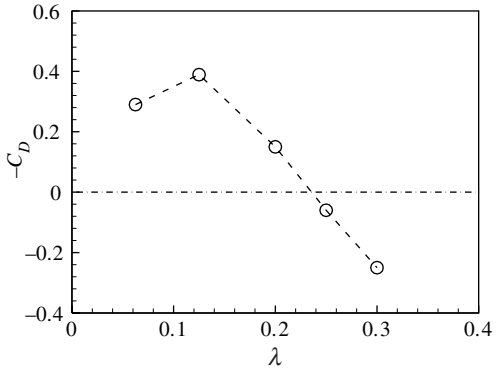

Fig. 13. Time-averaged drag coefficient versus the thickness ratio of the foil at $f = 1$ and $A_m = 0.16$

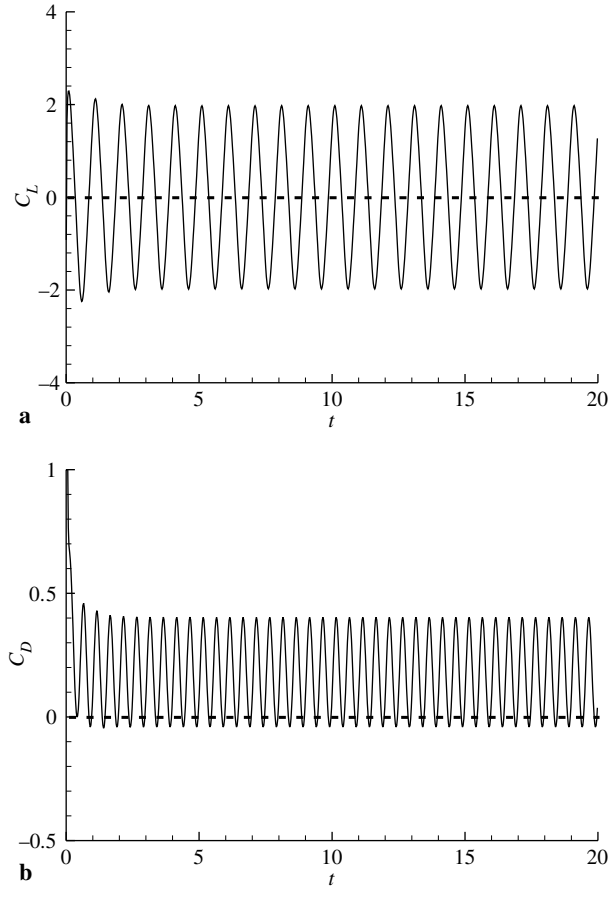

Fig. 14. Time-dependent lift and drag coefficients for the pitching oscillation at $\alpha_m = 10, f = 1$ and $\lambda = 0.125$: **a** lift coefficient C_L; **b** drag coefficient C_D

force behaviors are similar to Fig. 14 with an observation of the classic Karman vortex-street in the wake of the foil.

Finally, the viscous flow past an oscillating foil with coupled pitching and plunging motions is investigated. As a typical case, we first analyse the force behavior and vortex structures near the foil for $A_m = 0.16,\ \alpha_m = 5^\circ,\ \phi = 180^\circ,\ f = 1,\ \lambda = 0.125$. Figure 15 shows the time-dependent lift and drag coefficients. The time-averaged lift coefficient $\bar{C}_L$ is approximately zero, and the time-averaged drag coefficient $\bar{C}_D$ is negative to form a thrust force. To examine the feature of vortex shedding, the instantaneous vorticity contours, as shown in Fig. 16, exhibit

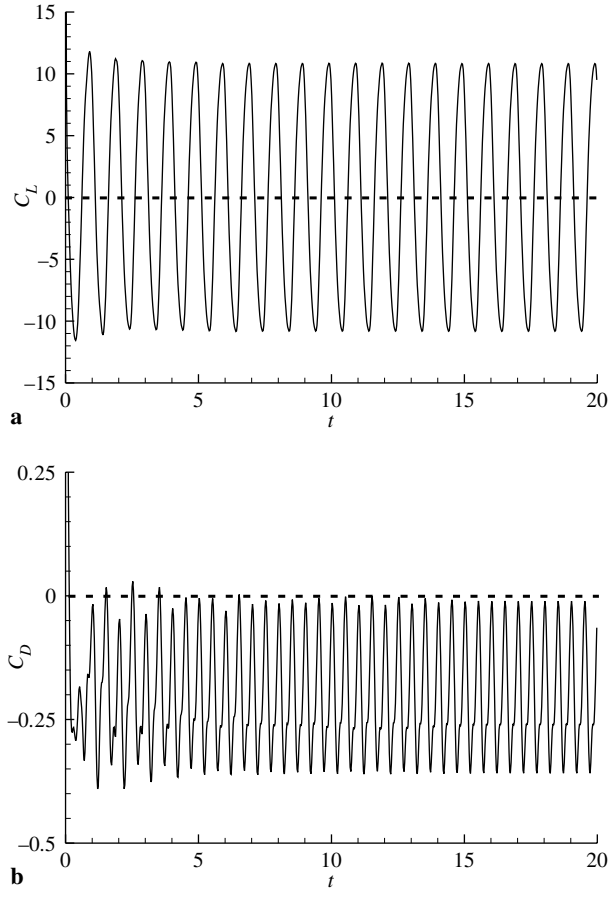

Fig. 15. Time-dependent lift and drag coefficients for the pitching oscillation at $A_m = 0.16$, $\alpha_m = 5°$, $\phi = 180°$, $f = 1$ and $\lambda = 0.125$: **a** lift coefficient C_L; **b** drag coefficient C_D

a reverse Karman vortex-street in the wake. It is also interesting to depict the vortex structures near the foil. Figure 17 shows the vorticity contours at several phases in one cycle. In Fig. 17a, when a negative leading-vortex LV_{N1} is generating, two vortex-pairs, i.e., $LV_{N0} + PLV_{N0}$ and $LV_{P0} + PLV_{P0}$, which are formed in the previous cycle, are moving downstream along the upper-side and lower-side of the foil, respectively. Then, the leading-vortex LV_{N1} induces an opposite sign vortex PLV_{N1} to form a vortex-pair (i.e., $LV_{N1} + PLV_{N1}$) in Fig. 17b. Meanwhile, a negative trailing-vortex TV_{N1} is generated and interacted with the vortex pair $LV_{N0} + PLV_{N0}$. In the following half-cycle, when the trailing-vortex TV_{N1} is shedding downstream, a positive leading-vortex LV_{P1} is generated in Fig. 17c. Then, the vortex LV_{P1} induces an opposite sign vortex PLV_{P1} to form a vortex-pair $LV_{P1} + PLV_{P1}$, which moves downstream along the lower-side of the foil (Fig. 17d). Meanwhile, when the vortex-pair $LV_{N1} + PLV_{N1}$ moves downstream along the upper-side of the foil, a positive trailing-vortex TV_{P1} is formed and interacted with the vortex-pair $LV_{P0} + PLV_{P0}$ in Fig. 17d. In this case, the leading-edge vortex evolution is a typical Mode-2 (Fig. 2b), and the reverse Karman vortex-street is formed in the near wake of the foil as shown in Fig. 16.

To deal with the effects of pitching and plunging amplitudes (i.e., α_m, A_m) and phase difference ϕ on the drag force (or thrust force), Fig. 18 shows the drag coefficient versus time for $\alpha_m = 5°$ and $10°$, $A_m = 0.08$ and 0.16, and $\phi = 90°$, $135°$ and $180°$. At $\phi = 135°$, as shown in Figs. 18a and c, an effective thrust force is generated, which is consistent with the previous experimental work [13]. However, at the plunging oscillation amplitude $A_m = 0.08$ (Fig. 18d),

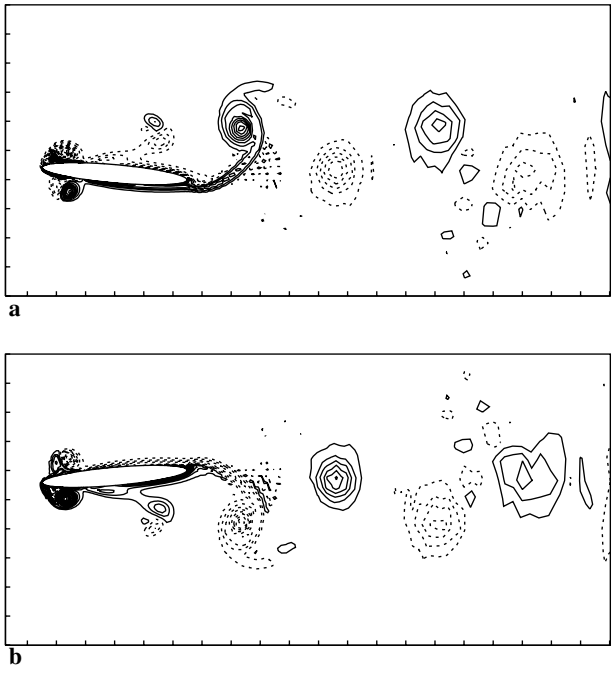

Fig. 16. Instantaneous vorticity contours at $A_m = 0.16$, $\alpha_m = 5^\circ$, $\phi = 180^\circ$, $f = 1$ and $\lambda = 0.125$: **a** $T/4$; **b** $3T/4$. Solid lines represent positive values and dashed lines negative values. The increment of the contours is 5

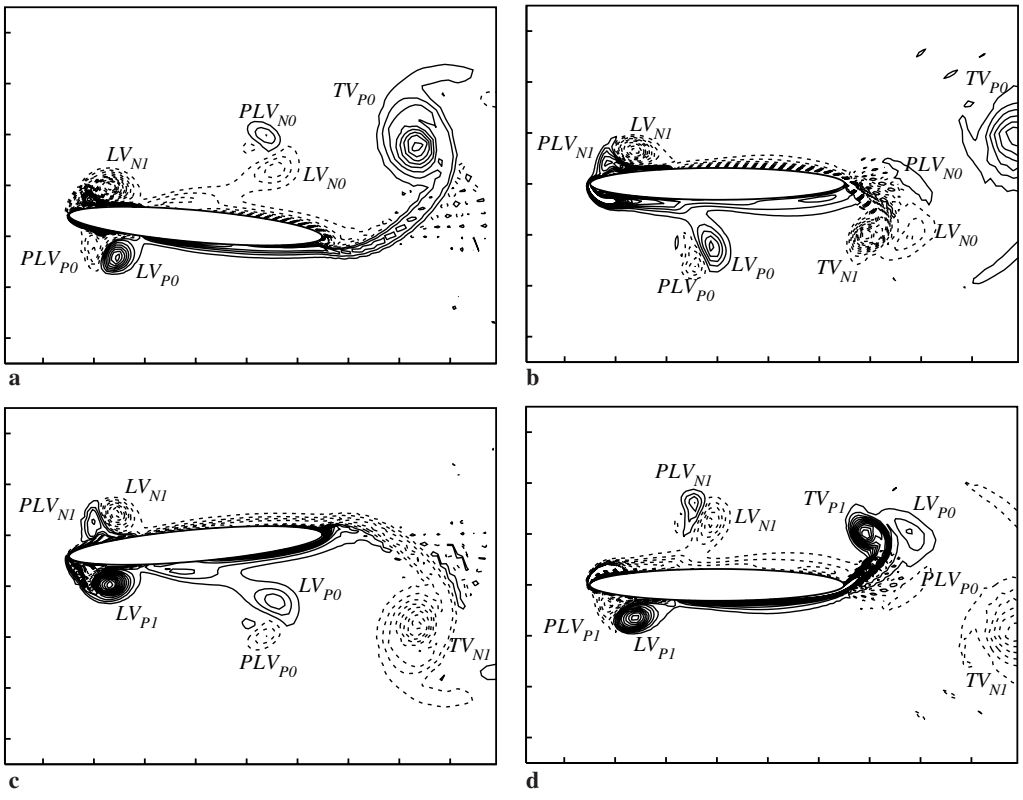

Fig. 17. Instantaneous vorticity contours at $A_m = 0.16$, $\alpha_m = 5^\circ$, $\phi = 180^\circ$, $f = 1$ and $\lambda = 0.125$: **a** $T/4$; **b** $2T/4$; **c** $3T/4$; **d** $4T/4$. Solid lines represent positive values and dashed lines negative values. The increment of the contours is 5

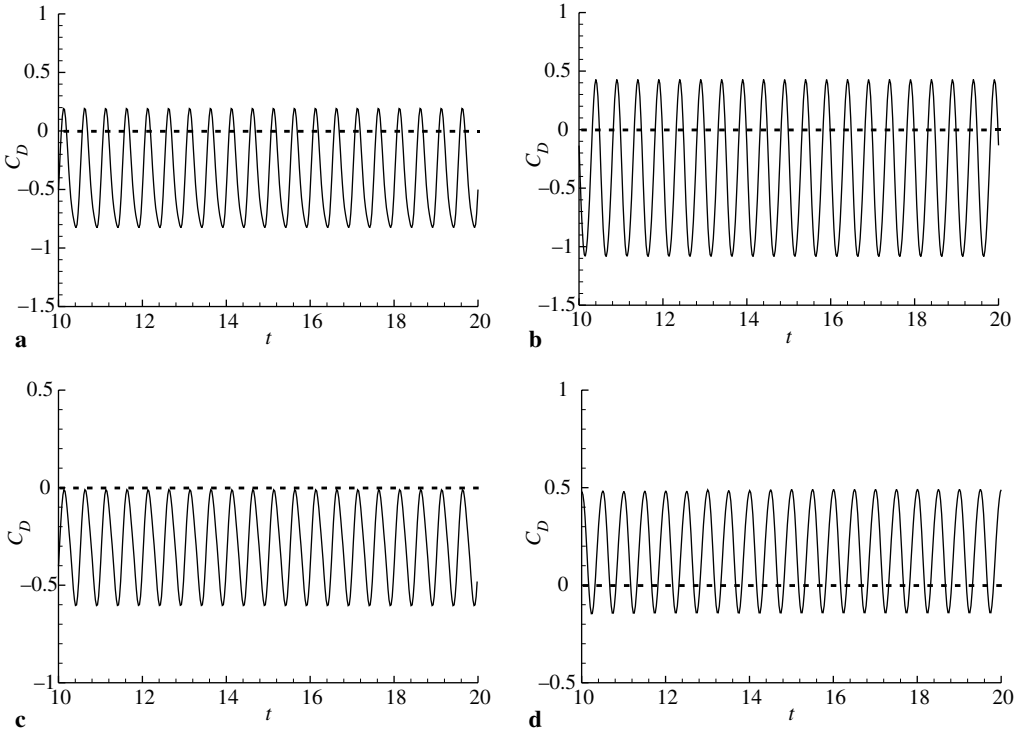

Fig. 18. Time-dependent drag coefficient at $f = 1$, $\lambda = 0.125$: **a** $A_m = 0.16$, $\alpha_m = 10^\circ$ and $\phi = 135^\circ$; **b** $A_m = 0.16$, $\alpha_m = 10^\circ$, $\phi = 90^\circ$; **c** $A_m = 0.16$, $\alpha_m = 5^\circ$, $\phi = 135^\circ$; **d** $A_m = 0.08$, $\alpha_m = 5^\circ$, $\phi = 180^\circ$

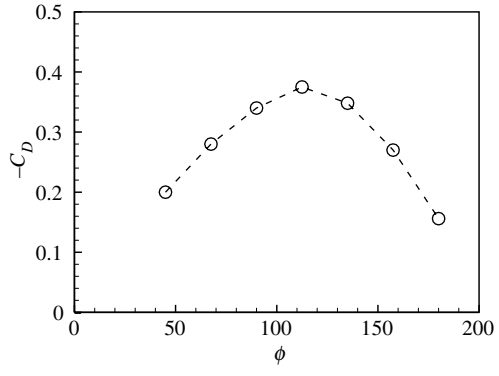

Fig. 19. Time-averaged drag coefficient versus the phase difference at $f = 1$, $\lambda = 0.125$, $A_m = 0.16$ and $\alpha_m = 10^\circ$

the time-averaged drag coefficient is positive. In a limiting case, when $A_m \to 0$, the foil motion is only the pitching oscillation, and a drag force is always generated as discussed in the above. According to the evolution of the vortex shedding (not shown here), the leading-edge vortex development in Fig. 18a–c behaves as the Mode-2 (Fig. 2b), and the reverse Karman vortex-street is formed in the near wake. However, the leading-edge vortex evolution in Fig. 18d behaves as the Mode-3 (Fig. 2c), and the Karman vortex-street is formed in the near wake.

As is well known, the phase difference ϕ is an important parameter for the generation of the drag force (or thrust force). To investigate the effect of the phase difference on the force, other parameters are chosen as $f = 1$, $\lambda = 0.125$, $A_m = 0.16$ based on possibly optimal parameter

selection from Figs. 8, 11 and 13. Then, Fig. 19 shows the time-averaged drag coefficient versus the phase difference at $f = 1$, $\lambda = 0.125$, $A_m = 0.16$ and $\alpha_m = 10°$. It is found that an effective thrust force is generated when the phase difference is $\phi = 75° \sim 150°$.

Finally, according to the present calculated results, as typically shown in Figs. 8, 11, 13 and 19, an optimal parameter combination to generate a high propulsive efficiency may be proposed as follows: the thickness ratio of the foil $\lambda = 0.1 \sim 0.15$, the plunging amplitude $A_m = 0.15 \sim 0.25$, the pitching amplitude $\alpha_m = 5° \sim 15°$, the frequency of the oscillation $f = 1 \sim 2$, and the phase difference $\phi = 75° \sim 150°$.

5 Concluding remarks

The propulsive performance and vortex shedding of a foil with the pitching and plunging oscillation are investigated by solving the two-dimensional incompressible Navier-Stokes equations in the vorticity and stream-function formulation. To accurately predict the force and vortex evolution, the fourth-order essentially compact finite difference schemes are employed to discretize the space derivatives and the fourth-order Runge-Kutta scheme to approximate the time advancement. Based on the present extensive calculation for a wide range of parameters, three types of the leading-edge vortex shedding evolution are identified and have an effective influence on the vortex shedding and vortex structures in the wake of the foil. The time-dependent drag and lift forces, in particular thrust force, and the relation of the force behavior with vortex structures near the foil and vortex shedding in the near wake are discussed. The effects of some typical factors, such as the frequency and amplitude of the oscillation, the phase difference, and the thickness ratio of the foil, on the vortex shedding and the corresponding time-dependent forces are analyzed. Based on the present calculated results, a possibly optimal parameter combination to generate a high propulsive efficiency is proposed. On the other hand, animal locomotion is certainly far more complex and diverse than the simple model considered here. Ideally, three-dimensional computation around an elastically flexible wing is desirable and is a target in our further work.

Acknowledgements

This work was supported by the National Natural Science Foundation (No.10125210, 10072063), the Innovation Project of the Chinese Academy of Sciences (No. KJCX-SW-L04, KJCX2-SW-L2), and the Hundred-Talent Programme of the Chinese Academy of Sciences.

References

[1] Weis-Fogh, T., Jensen, M.: Biology and physics of locust flight. Proc. Roy. Soc. B. **239,** 415–585 (1956).
[2] Lighthill, M. J.: Mathematical biofluiddynamics. Philadelphia: SIAM 1975.
[3] Lighthill, M. J.: Aquatic animal propulsion of high hydromechanical efficiency. J. Fluid Mech. **44,** 265–301 (1970).
[4] Maxworthy, T.: The fluid dynamics of insect flight. Ann. Rev. Fluid Mech. **13,** 329–354 (1981).
[5] Ellington, C. P.: The aerodynamics of hovering insect flight. Phil. Trans. Roy. Soc. Lond. B **305,** 1–21 (1984).

[6] Spedding, G. R.: The aerodynamics of flight. In: Mechanics of animal locomotion (Alexander. R. M, ed.), p. 51. New York: Springer 1992.
[7] Shyy, W., Berg, M., Ljungqvist, D.: Flapping and flexible wings for biological and micro air vehicles. Prog. Aerospace Sci. **35,** 455–505 (1999).
[8] Phlips, P. J., East, R. A., Pratt, N. H.: An unsteady lifting line theory of flapping wings with application to the forward flight of birds. J. Fluid Mech. **112,** 97–125 (1981).
[9] Chopra, M. G.: Large amplitude lunate-tail theory of fish locomotion. J. Fluid Mech. **74,** 161–182 (1976).
[10] Cheng, J. Y., Zhuang, L. X., Tong, B. G.: Analysis of swimming 3-D waving plate. J. Fluid Mech. **232,** 341–355 (1991).
[11] Smith, M. J. C., Wilkin, P. J., Williams, M. H.: The advances of an unsteady method in modeling the aerodynamic forces on rigid flapping wings. J. Expl. Biol. **199,** 1073–1083 (1996).
[12] Triantafyllou, M. S., Triantafyllou, G. S., Gopalkrishnan, R.: Wake mechanics for thrust generation in oscillation foils. Phys. Fluids **3,** 12–26 (1991).
[13] Anderson, J. M., Streitlien, K., Barrett, D. S., Triantafyllou, M. S.: Oscillating foils of high propulsive efficiency. J. Fluid Mech. **360,** 41–72 (1998).
[14] Gursul, I., Ho, C.-M.: Oscillating foils of high propulsive efficiency. AIAA J. **30,** 1117–1124 (1992).
[15] Ellington, C. P., Berg, C. van den, Willmott, A. P., Thomas, A. L. R.: Leading-edge vortices in insect flight. Nature **384,** 626–630 (1996).
[16] Dickinson, M. H., Lehmann, F. O., Sane, S. P.: Wing rotation and the aerodynamic basis of insect flight. Science **284,** 1954–1960 (1999).
[17] Van den Berg, C., Ellington, C. P.: The vortex wake of a hovering model hawkmoth. Phil. Trans. R. Soc. Lond. B **352,** 317–328 (1997).
[18] Birch, J. M., Dickinson, M. H.: Spanwise flow and the attachment of the leading-edge vortex on insect wings. Nature **412,** 729–733 (2001).
[19] Srygley, R. B., Thomas, A. L. R.: Unconventional lift-generating mechanism in free-flying butterflies. Nature **420,** 660–664 (2002).
[20] Gustafson, K. E., Leben, R.: Computation of dragonfly aerodynamics. Comp. Phys. Commun. **65,** 121–129 (1991).
[21] Liu, H., Kawachi, K.: A numerical study of insect flight. J. Comp. Phys. **146,** 124–143 (1998).
[22] Liu, H., Ellington, C. P., Kawachi, K., Berg, C. van den, Willmott, A. P.: A computational fluid dynamics study of hawkmoth hovering. J. Exp. Biol. **201,** 461–477 (1998).
[23] Wang, J.: Vortex shedding and frequency selection in flapping flight. J. Fluid Mech. **410,** 323–341 (2000).
[24] Hall, K. C., Pigott, S. A., Hall, S. R.: Power requirements for large-amplitude flapping flight. J. Aircraft **35,** 352–359 (1998).
[25] Sun, M., Tang, J.: Unsteady aerodynamic force generation by a model fruit fly wing in flapping motion. J. Exp. Biol. **205,** 55–70 (2002).
[26] Sun, M., Tang, J.: Lift and power requirements of hovering flight in Drosophila virilis. J. Exp. Biol. **205,** 2413–2427 (2002).
[27] E, W., Liu, J. G.: Essentially compact schemes for unsteady viscous incompressible flows. J. Comp. Phys. **126,** 122–138 (1996).
[28] Wu, J. Z., Lu, X. Y., Wu, J. M.: Post-stall flow control on an airfoil by local unsteady forcing. J. Fluid Mech. **371,** 21–58 (1998).
[29] Norberg, R. A.: Hovering flight of the dragonfly Aeschna juncea L., kinematics and dynamics. In: Swimming and flying in nature (Wu, T. Y., Brokaw, C. J., Brennen, C., eds.), vol. 2, p. 763. New York: Plenum 1975.
[30] Lu, X. Y., Dalton, C.: Calculation of the timing of vortex formation from an oscillating cylinder. J. Fluids Struct. **10,** 527–541 (1996).

Authors' address: X.-Y. Lu, J.-M. Yang and X.-Z. Yin, Department of Modern Mechanics, University of Science and Technology of China, Hefei, Anhui 230026, P. R. China (E-mail: xlu@ustc.edu.cn)